Resonant Rayleigh scattering from an anisotropic organic single-crystal microcavity

S. Kéna-Cohen,[1,2] M. Davanço,[2] and S. R. Forrest[2,*]
[1]*Department of Electrical Engineering, Princeton Institute for the Science and Technology of Materials (PRISM), Princeton University, Princeton, New Jersey 08544, USA*
[2]*Departments of Electrical Engineering and Computer Science and Physics, University of Michigan, Ann Arbor, Michigan 48109, USA*
(Received 11 July 2008; revised manuscript received 9 September 2008; published 6 October 2008)

Resonant Rayleigh scattering (RRS) is observed upon excitation of a microcavity containing a single crystal of the organic molecule anthracene. The RRS profile is obtained for a range of excitation energies and angles. In contrast to the circular profile observed for inorganic microcavities, the scattered light pattern is elliptical when projected normal to the sample surface. The profile shape provides a direct visual representation of the anisotropic microcavity polariton dispersion characteristic of organic crystals.

DOI: 10.1103/PhysRevB.78.153102 PACS number(s): 71.36.+c, 71.35.Aa, 72.80.Le

Rayleigh scattering from semiconductors typically results from structural imperfections that cause local fluctuations in the refractive index. Hegarty *et al.*[1] noted that resonant Rayleigh scattering (RRS) can be used to obtain information about electronic resonances in the presence of disorder. In that case, the homogeneous linewidth of an inhomogeneously broadened GaAs quantum well was extracted by fitting the energy dependence of the scattered light intensity. Since then, there have been several studies of time-averaged and time-resolved RRS from inorganic semiconductor quantum wells and semiconductor microcavities.[2–6] These have been used to study the role of disorder and to extract dephasing times for the excitations. Here, we observe RRS from an anisotropic organic single-crystal microcavity and find that it provides a direct visual representation of the anisotropic polariton dispersion.

Upon resonant excitation of a semiconductor by laser light, secondary emission at the excitation wavelength can occur either due to RRS or to resonant photoluminescence (PL).[7] In the absence of disorder, coherent re-emission can only occur in the specular transmission and reflection directions. However, phase-preserving elastic scattering, such as that from static disorder, leads to re-emission by RRS in other directions. Hence, RRS remains coherent with the excited interband polarization, and for single-scattering processes, retains the polarization direction of the exciting laser light. Resonant PL, however, occurs from decay of the interband polarization through phase-destroying mechanisms and is incoherent with the exciting laser beam.

In semiconductor microcavities where the light-matter interaction is stronger than the damping of both the cavity photon and exciton, an anticrossing of the normal modes occurs at the degeneracy point.[8] The new eigenstates of the system, cavity polaritons, form a coherent superposition of both the cavity photon and exciton. Unlike bare excitons that possess a flat dispersion below the light line, the dispersion of the lower polariton branch exhibits significant curvature up to the degeneracy point due to its cavity photon content. As a result, the elastic-scattering contours in an isotropic semiconductor microcavity form circular rings in k-space as dictated by conservation of in-plane momentum, and these can be directly observed in the RRS profile.[2–4] The ring radius is given by the resonance condition, while its width is determined by the broadening of the polariton dispersion in k- space.

In crystalline organic semiconductor microcavities, the situation is more complicated. Typically, organic crystalline solids contain two molecules per unit cell, in which case the intermolecular interaction leads to a splitting of the excitonic resonance into two Davydov components.[9] In anthracene, for example, the lowest-lying transition lies along the short axis of the molecule, and in the crystal phase it is split into two moderately intense transitions lying parallel and perpendicular to the monoclinic **b** axis [see Fig. 1(a)]. These excitonic resonances couple to a cavity photon which is also anisotropic due to differences in the background refractive index originating from higher lying electronic transitions. An anisotropic polariton dispersion relation is thus expected, depending on both the incidence (θ) and the azimuthal (ϕ) angles, as shown in Fig. 1(b). Understanding this dispersion is crucial for the investigation of nonlinear parametric processes.

In principle, the anisotropic microcavity dispersion can be

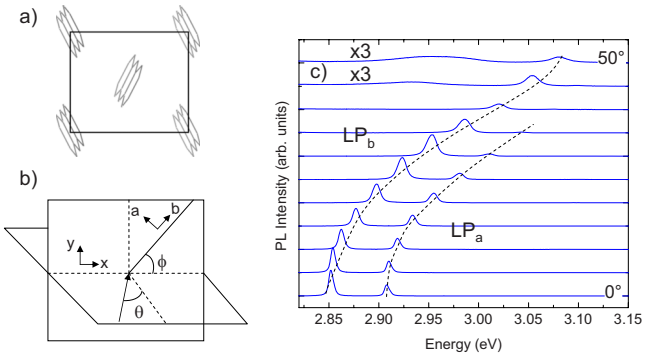

FIG. 1. (Color online) (a) Projection of the anthracene monoclinic unit cell viewed along the **c** crystal axis. (b) Experimental arrangement showing the incident (θ) and azimuthal (ϕ) angles. The azimuthal angle is defined as the angle between the **b** crystal axis and the plane of incidence. The cavity was excited such that $\phi=0$ and with **b** along the **x** laboratory axis. (c) Angle-resolved nonresonant photoluminescence from the microcavity measured along $\phi=0$. The lowest energy branch corresponds to LP_b and the other branch to LP_a. The spectra are given in 5° increments.

extracted from angle-resolved reflectivity, transmission, or photoluminescence measurements versus both incidence and azimuthal angles. Equivalently, by mapping the RRS pattern, the full dispersion can be directly visualized and the effects of anisotropy can be gauged by observing the shape of the elastic-scattering contours. We find that the anisotropy is especially pronounced for large values of in-plane momenta, consistent with theory,[10,11] but that the strongest effect comes from differences in background refractive index along the different crystal axes.

The sample consists of 140 nm thick, 0.5 mm wide by approximately 2 cm long channels of single-crystal anthracene sandwiched between two distributed Bragg reflectors (DBRs) composed of 12 pairs of SiO_2/SiN_x. X-ray diffraction confirmed that stacking of the crystals occurred in the (001) direction with the **ab** plane lying parallel to the substrate. The fabrication and angle-resolved reflectivity spectra of this structure are reported elsewhere.[12] For the RRS measurements, a tunable Ti:sapphire laser producing 200 fs pulses with a repetition rate of 76 MHz was used. The laser output was frequency doubled by a 1 mm thick β-BaB_2O_4 crystal and then filtered using a dichroic mirror. This generated tunable pulses spanning the entire range of energies of the lower polariton branch. The RRS pattern was projected onto a screen oriented normal to the sample surface in a transmission geometry and captured using a charge coupled device (CCD) camera. The half-angle spread in the angle of incidence was $\sim 0.5°$ for θ and ϕ. For continuous-wave (CW) measurements, the sample was nonresonantly excited at a wavelength of $\lambda = 325$ nm from a HeCd laser.

Figure 1(c) shows angle-resolved PL measured along the $\phi = 0$ direction under nonresonant CW excitation. Only the lower polariton branches are observed in PL. The lowest energy branch (LP_b) corresponds to the **b** exciton and the other (LP_a) to the **a** exciton. The PL originating from LP_b and LP_a is linearly polarized along the **b** and **a** crystal axes, respectively, regardless of sample orientation. This is in contrast to the situation in inorganic semiconductor microcavities where the normal modes can be separated into TE and TM polarizations and no rotational dependence is observed. The dispersion extracted along $\phi = 0$ from angle-resolved PL and reflectivity[12] is shown in Fig. 2. Note that for $\theta > 60°$, the DBRs become transparent and the lower polariton branches vanish.

The lower branches were resonantly excited with in-plane momentum $k_\parallel = (k_x, 0)$ (corresponding to $\phi = 0$) by selecting the appropriate polarization (TE for LP_a and TM for LP_b), energy, and angle θ. The RRS pattern obtained for particular angles and energies is shown in Fig. 3. The speckle, which is observed in all patterns, suggests that the emission is mostly coherent, thereby justifying the assignment to RRS. We note that the polarized resonant PL and the RRS makes it impossible to clearly distinguish between the two in a time-averaged measurement based solely on the degree of polarization with respect to the exciting laser. Indeed, regardless of the scattering direction, the emission is always polarized along the crystal axis corresponding to the excited polariton. From Fig. 3, it is observed that the RRS pattern corresponding to LP_a is nearly circular, while that corresponding to LP_b possesses significant asymmetry leading to an elliptical

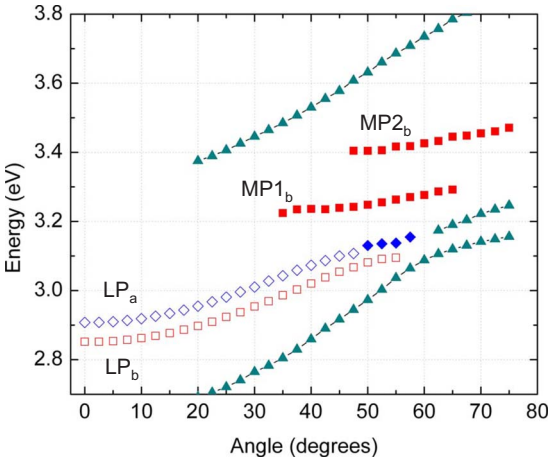

FIG. 2. (Color online) Dispersion along the $\phi = 0$ direction extracted from the peak positions of the angle-resolved PL (hollow symbols) and reflectivity dip positions from Ref. 12 (filled symbols). The middle polariton branch (MP1 and MP2) dispersions are also shown. The triangles correspond to the edges of the DBR stop band (reflectivity minima).

shape. This asymmetry increases as the incidence angle (and energy) is increased. The bright spot in the patterns corresponds to the directly transmitted beam, which is blocked in Fig. 3(d) to avoid saturating the CCD.

Upon laser excitation, a coherent polarization $P_{kx0,ky0}$ is created. Polarization transfer from disorder scattering can occur to $P_{kx,ky}$ if the final momentum vectors of the scattered polarization lie on the elastic-scattering surface determined by the dispersion relation. The dispersion relation of crystalline organic microcavities has previously been derived for the case of perfect mirrors and two molecules per unit cell.[10,11] It was shown that some weak mixing on the order of $(k_\parallel/Q)$ (Ref. 4) occurs between the two Davydov components, where $k_\parallel$ is the in-plane wave vector and Q is the total wave vector. Neglecting mixing, the lower polariton dispersion for each branch is independent and given by

$$E_{\mathrm{LP}a,\mathrm{LP}b} = \frac{E_{a,b}^{\mathrm{ex}}(k) + E_k^{\mathrm{cav}}}{2} - \sqrt{\left[\frac{E_{a,b}^{\mathrm{ex}}(k) - E_k^{\mathrm{cav}}}{2}\right]^2 + V_{a,b}^2\left(1 - \frac{k_\parallel^2}{Q^2} f(\phi)\right)}. \quad (1)$$

Here, $E_{\mathrm{LP}a}$ ($E_{\mathrm{LP}b}$) is the energy of the lower polariton branch corresponding to the ***a*** (***b***) exciton, $E_a^{\mathrm{ex}}(k)$ [$E_b^{\mathrm{ex}}(k)$] is the Coulomb exciton[13] energy, $E_{\mathrm{cav}}(k)$ is the cavity photon energy, $V_{a,b}$ is the interaction potential, and $f(\phi) = \cos^2(\phi)[\sin^2(\phi)]$. We see that anisotropy is pronounced only for large values of the in-plane momentum $k_\parallel$ and results in a ϕ-dependent expression for the Rabi splitting and Coulomb exciton energy. It was also pointed out[11] that the polaritons are composed of a combination of TE and TM modes such that the LP_a and LP_b polaritons are almost completely polarized along the **a** and **b** crystal axes, respectively, which is consistent with our observations. For anthracene,

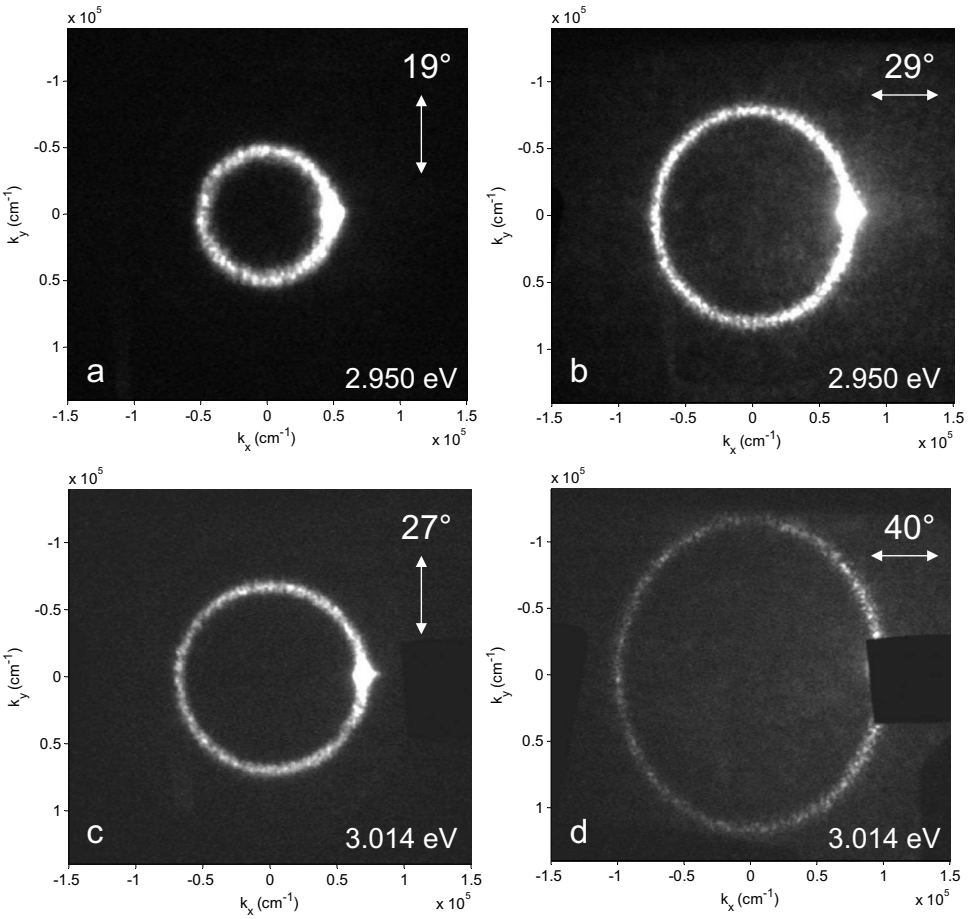

FIG. 3. Resonant Rayleigh scattering images projected onto a screen oriented perpendicular to the sample surface in a transmission geometry. The excitation angle, polarization direction, and energy of the exciting laser are indicated in the inset of each image. The bright spot corresponds to the straight through beam and is blocked in (d) to avoid saturating the CCD. (a) and (c) show LP_a, while (b) and (d) show LP_b. The direction of excitation was chosen such that $k_y=0$. Note the increase in ellipticity as the in-plane momentum is increased. The (k_x,k_y) scale is indicated on all of the images, where the scale bar ranges from (0,0) to $(1.5,1.4)\times 10^5$ cm^{-1}.

mixing of the intramolecular vibronics contributes to the lower branch dispersion. The theory can be extended to this case, but the ellipticity which results from using the analog of Eq. (1) is much smaller than experimentally observed.

The differences occur due to anisotropies in the photonic component of the cavity arising from the different background (i.e., nonresonant) refractive index along each crystal axis. This leads to an elliptical dispersion relation for the Fabry-Perot cavity mode and accounts for the largest fraction of the ellipticity of the RRS contours. We have calculated the dispersion relation of our structure based on an anisotropic transfer matrix that consists of propagating the in-plane components of the electric and magnetic fields along the various interfaces according to first-order Maxwell equations.[14,15] An orthorhombic dielectric tensor was used with $\varepsilon_{z0}=2.9$, while $\varepsilon_{y0}\equiv\varepsilon_a$ and $\varepsilon_{x0}\equiv\varepsilon_b$ were taken from Ref. 16. An exact calculation accounting for the monoclinic structure would require knowledge of the frequency dependent Euler angles. Nominal measured film thicknesses were used and no parameters were fitted. The method fully accounts for the response of the (isotropic) DBRs and, in particular, the polarization dependence of the penetration depth.

The in-plane electric- and magnetic-field components $\Psi=(E_x,E_y,H_x,H_y)^T$ across a layer of thickness h are calculated as $\Psi(z+h)=\exp(i\omega h\boldsymbol{\Delta}/c)\Psi(z)$, where ω is the angular frequency and c is the speed of light in vacuum. For laboratory coordinates oriented such that the in-plane momentum $k_\parallel$ is along x:

$$\Delta=\begin{pmatrix} -k_\parallel\frac{\varepsilon_{31}}{\varepsilon_{33}} & -k_\parallel\frac{\varepsilon_{32}}{\varepsilon_{33}} & 0 & 1-\frac{k_\parallel^2}{\varepsilon_{33}} \\ 0 & 0 & -1 & 0 \\ \varepsilon_{23}\frac{\varepsilon_{31}}{\varepsilon_{33}}-\varepsilon_{21} & k_\parallel^2-\varepsilon_{22}+\varepsilon_{23}\frac{\varepsilon_{32}}{\varepsilon_{33}} & 0 & k_\parallel\frac{\varepsilon_{23}}{\varepsilon_{33}} \\ \varepsilon_{11}-\varepsilon_{13}\frac{\varepsilon_{31}}{\varepsilon_{33}} & \varepsilon_{12}-\varepsilon_{13}\frac{\varepsilon_{32}}{\varepsilon_{33}} & 0 & -k_\parallel\frac{\varepsilon_{23}}{\varepsilon_{33}} \end{pmatrix}. \quad (2)$$

The dielectric tensor in this coordinate system is obtained by an Euler rotation of the intrinsic (diagonal) dielectric tensor $\boldsymbol{\varepsilon}_0$, such that $\boldsymbol{\varepsilon}=\boldsymbol{A}\boldsymbol{\varepsilon}_0\boldsymbol{A}^{-1}$, where $\boldsymbol{A}$ is the Euler rotation matrix. The assignment can then be made that $k_x=k_\parallel\sin\theta\cos\phi$ and $k_y=k_\parallel\sin\theta\sin\phi$. We note that when the intrinsic coordinate system of the crystal is aligned with the laboratory axes ($\phi=0°$ or 90°),[14] it is possible to decompose the field into TE and TM components to obtain simple expressions for the propagation vectors. In general, however, Δ must be diagonalized to calculate the wave polarization.

To calculate the dispersion, it is convenient to rewrite the transfer matrix in the same form as that given in Ref. 17:

$$\begin{pmatrix} A_s \\ B_s \\ A_p \\ B_p \end{pmatrix}=\begin{pmatrix} M_{11} & M_{12} & M_{13} & M_{14} \\ M_{21} & M_{22} & M_{23} & M_{24} \\ M_{31} & M_{32} & M_{33} & M_{34} \\ M_{41} & M_{42} & M_{43} & M_{44} \end{pmatrix}\begin{pmatrix} C_s \\ 0 \\ C_p \\ 0 \end{pmatrix}, \quad (3)$$

where A and B are the field amplitudes of the incident and reflected waves, respectively, and C is the amplitude of the transmitted wave. The dispersion can then be found by solv-

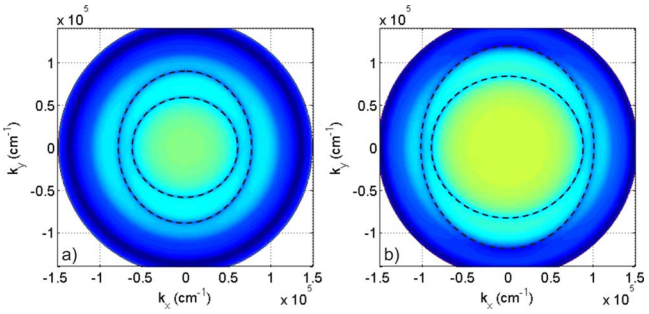

FIG. 4. (Color online) Calculated dispersion for the energies corresponding to Fig. 3. (a) 2.950 eV and (b) 3.014 eV. These patterns are obtained by directly plotting $F(\omega,k_x,k_y)=M_{11}M_{33}-M_{13}M_{31}$, with M_{ij} defined in Eq. (3). The contours are plotted using a logarithmic color scale to reduce the contrast. The dark regions correspond to the minima and dashed lines were added for clarity. The contours corresponding to both lower polariton branches are evident in each figure. The outer circle corresponds to the edge of the light cone. The scale used is the same as in Fig. 3 to facilitate comparison.

ing for the poles of the reflectance (or transmittance), i.e., $F(\omega,k_x,k_y)=M_{11}M_{33}-M_{13}M_{31}=0$. This function is plotted in Fig. 4 for the energies corresponding to the RRS patterns of Fig. 3. The normal modes corresponding to both LP_a and LP_b can be identified as the minima in both figures, and these agree with experiment. Strictly speaking, since the full refractive index was used, ω should be extended to the complex plane to calculate the true dispersion. However, since in this energy range the damping of the polaritons is small, the correction in using the real-valued minima is expected to be correspondingly negligible.

We have observed RRS from a microcavity containing a single crystal of the organic molecule anthracene. We have found that the RRS pattern provides a direct visualization of the anisotropic polariton dispersion and that the strongest contribution to the ellipticity comes from the photonic component of the cavity. The dispersion of the full structure was numerically calculated by solving for the poles of the scattering amplitude and the resulting contours were found to correspond to the experimentally observed RRS patterns. The plasma-enhanced chemical vapor deposition grown DBRs are known to have significant interface roughness and these are likely to play a major role in the disorder-induced scattering observed. Also, the inhomogeneities and crystal strain resulting from the melt-grown anthracene are largely undetermined and cannot be probed directly by x-ray due to the enclosing substrates. This may, therefore, warrant further investigation of RRS of the exciton localization in melt-grown anthracene crystals.

This work was performed at the Lurie Nanofabrication Facility at the University of Michigan. The authors acknowledge Universal Display Corp. and the Air Force Office of Scientific Research for partial financial support. S.K.-C. acknowledges support from the Fonds Québecois sur la Nature et les Technologies.

*Corresponding author: stevefor@umich.edu

[1] J. Hegarty, M. D. Sturge, C. Weisbuch, A. C. Gossard, and W. Wiegmann, Phys. Rev. Lett. **49**, 930 (1982).
[2] T. Freixanet, B. Sermage, J. Bloch, J. Y. Marzin, and R. Planel, Phys. Rev. B **60**, R8509 (1999).
[3] R. Houdre, C. Weisbuch, R. P. Stanley, U. Oesterle, and M. Ilegems, Phys. Rev. B **61**, R13333 (2000).
[4] W. Langbein and J. M. Hvam, Phys. Rev. Lett. **88**, 047401 (2002).
[5] W. Langbein, J. M. Hvam, and R. Zimmermann, Phys. Rev. Lett. **82**, 1040 (1999).
[6] H. Stolz, D. Schwarze, W. von der Osten, and G. Weimann, Phys. Rev. B **47**, 9669 (1993).
[7] J. Shah, *Ultrafast Spectroscopy of Semiconductors and Semiconductor Nanostructures* (Springer, Berlin, 1999).
[8] C. Weisbuch, M. Nishioka, A. Ishikawa, and Y. Arakawa, Phys. Rev. Lett. **69**, 3314 (1992).
[9] A. S. Davydov, *Theory of Molecular Excitons* (Plenum, New York, 1971).
[10] H. Zoubi and G. C. La Rocca, Phys. Rev. B **71**, 235316 (2005).
[11] M. Litinskaya, P. Reineker, and V. M. Agranovich, Phys. Status Solidi A **201**, 646 (2004).
[12] S. Kena-Cohen, M. Davanço, and S. R. Forrest, Phys. Rev. Lett. **101**, 116401 (2008).
[13] V. M. Agranovich and V. L. Ginzburg, *Crystal Optics with Spatial Dispersion, and Excitons* (Springer-Verlag, Berlin, 1984).
[14] D. W. Berreman, J. Opt. Soc. Am. **62**, 502 (1972).
[15] M. Schubert, Phys. Rev. B **53**, 4265 (1996).
[16] A. Matsui and Y. Ishii, J. Phys. Soc. Jpn. **23**, 581 (1967).
[17] P. Yeh, Surf. Sci. **96**, 41 (1980).